The Astronomical Journal, 160:42 (15pp), 2020 July https://doi.org/10.3847/1538-3881/ab9608

Two Strengths of Ordinary Chondritic Meteoroids as Derived from Their Atmospheric Fragmentation Modeling

Jiří Borovička, Pavel Spurný, and Lukáš Shrbený
Astronomical Institute of the Czech Academy of Sciences, Fričova 298, CZ-25165 Ondřejov, Czech Republic; jiri.borovicka@asu.cas.cz
Received 2020 February 24; revised 2020 May 14; accepted 2020 May 22; published 2020 June 25

Abstract

The internal structure and strength of small asteroids and large meteoroids is poorly known. Observation of bright fireballs in the Earth's atmosphere can explore meteoroid structure by studying meteoroid fragmentation during the flight. Earlier evaluations showed that the meteoroid's strength is significantly lower than that of the recovered meteorites. We present a detailed study of atmospheric fragmentation of seven meteorite falls, all ordinary chondrites, and 14 other fireballs, where meteorite fall was predicted but the meteorites, probably also ordinary chondrites, were not recovered. All observations were made by the autonomous observatories of the European Fireball Network and include detailed radiometric light curves. A model, called the semiempirical fragmentation model, was developed to fit the light curves and decelerations. Videos showing individual fragments were available in some cases. The results demonstrated that meteoroids do not fragment randomly but in two distinct phases. The first phase typically corresponds to low strengths of 0.04–0.12 MPa. In two-thirds of cases, the first phase was catastrophic or nearly catastrophic with at least 40% of mass lost. The second phase corresponds to 0.9–5 MPa for confirmed meteorite falls and somewhat lower strengths, from about 0.5 MPa, for smaller meteoroids. All of these strengths are lower than the tensile strengths of ordinary chondritic meteorites cited in the literature, 20–40 MPa. We interpret the second phase as being due to cracks in meteoroids and the first phase as a separation of weakly cemented fragments, which reaccumulated at the surfaces of asteroids after asteroid collisions.

Unified Astronomy Thesaurus concepts: Meteoroids (1040); Meteorites (1038); Asteroids (72); Fireballs (538); Near-Earth objects (1092); Impact phenomena (779)

1. Introduction

There are two main methods of studying interplanetary material in the vicinity of the Earth: astronomical and geochemical. The astronomical method relies primarily on telescopic observations of asteroids and comets from both the ground and space. In favorable cases, optical observations can be supplemented by radar investigation. The obtained data include orbits, rotational properties, shapes, albedos, sizes, and reflectance spectra of asteroids. For active comets, their emission spectra and properties of the released gases and dust can be obtained. The geochemical method is applicable only to meteorites and, in a few recent cases, to samples returned by spacecraft. The advantage is that the mineralogical, chemical, and physical properties of meteorites and returned samples can be studied in the laboratory in detail.

Of particular interest are the physical properties and internal structure of asteroids. Knowledge of them is important to understand evolutionary history of asteroids, and the inner solar system in general, as well as to evaluate the consequences of potential asteroid collision with the Earth. Physical properties are also to be considered in any attempt at deflecting an asteroid from impact trajectory or in an effort toward asteroid mining. Telescopic observations, however, provide limited information about the internal structure of asteroids. The existence of a spin barrier at the rotation period of 2.4 hr was revealed for asteroids in a size range from ∼200 m to ∼10 km (Pravec & Harris 2000; Hestroffer et al. 2019), suggesting that most asteroids in this size range may be aggregates of smaller blocks held together only by their mutual gravity: so-called rubble piles. Asteroids smaller than 200 m have a wide range of rotational periods, and their internal strength is not restricted by these observations.

The most common type of meteorites, ordinary chondrites, which represent 81% of all meteorite falls (Borovička et al. 2019a), are hard objects. Individual measured strengths vary widely; nevertheless, typical compressive strengths are between 100 and 200 MPa and tensile strengths are between 20 and 40 MPa, i.e., comparable to the strongest terrestrial rocks (Slyuta 2017; Flynn et al. 2018; Ostrowski & Bryson 2019). Meteorites are delivered by meteoroids and small asteroids in a size range from decimeters to decameters (hereafter collectively called "meteoroids") and represent their strongest parts, which survived the atmospheric passage. It is well known that meteoroids are subject to fragmentation during their interaction with the atmosphere. The sole fact that the vast majority of meteorite falls produce more than one meteorite, sometimes of the order of a thousand pieces (e.g., Jenniskens et al. 1994; Fry et al. 2013), is sufficient proof of meteoroid atmospheric fragmentation. Incoming meteoroids are therefore weaker than recovered meteorites.

In this work, we use atmospheric fragmentation to evaluate the strengths of meteoroids. This idea is not new. Fadeenko (1967), among the first, considered that meteoroids will fragment when the dynamic pressure acting on the leading surface,

$$p = \rho v^2, \tag{1}$$

where ρ is atmospheric density and v is meteoroid velocity, exceeds the strength of the material. Other authors used the same relation when either modeling the meteoroid atmospheric entry (e.g., Baldwin & Sheaffer 1971; Hills & Goda 1993; Svetsov et al. 1995; Bland & Artemieva 2006; Register et al. 2017) or inferring meteoroid strengths from observations (e.g., Trigo-Rodríguez & Llorca 2006; Popova et al. 2011). Note that

the meteoroid strength is not precisely defined in this approach. Various types of material strength were discussed by Holsapple (2009). The fragmentation strength derived from the dynamic pressure is usually considered to correspond to the tensile strength of the material (e.g., Trigo-Rodríguez & Llorca 2006), but a recent calculation showed that the shear strength may be the most relevant, at least for large bodies (Robertson & Mathias 2017).

Ceplecha et al. (1993) studied the fragmentation of 51 fireballs photographed by the US Prairie Network. Only fireball dynamic data, i.e., lengths along the trajectory as a function of time, were used. Fragmentations were therefore found on the basis of increased deceleration after a sudden mass loss. The method was able to reveal one dominant fragmentation point in 19 cases. Eleven fireballs produced so-called inverse solutions, which were interpreted as multifragmentation events. The positions of the fragmentations could not be found in these cases. The strengths for single fragmentation events were found in the range 0.05–1.2 MPa. One exceptional meteoroid survived without significant fragmentation up to 5 MPa.

Popova et al. (2011) evaluated fragmentation in 11 instrumentally observed meteorite falls. Fragmentation data were compiled from original sources. The used data set was therefore very heterogeneous, with fireball data of varying quality obtained by various techniques. Various signatures were used to reveal fragmentation points along the trajectory. The resulting message was, nevertheless, clear. Incoming meteoroids and small asteroids have very low strengths in comparison with meteorites.

In this paper, we compile analyses of seven instrumentally observed falls of ordinary chondrites (one is the same as in Popova et al. 2011; six are new). In all cases, the fireball data are sufficient for detailed fragmentation modeling. In addition to known trajectories and velocities, radiometric light curves with high temporal resolution and dynamic range are available. In some cases, dynamic data, i.e., fireball decelerations, are also available along the whole trajectories. In addition, we analyze 14 other fireballs, which certainly also dropped meteorites of masses of at least several tens of g, but the meteorites were, unfortunately, not recovered. In these cases, both radiometric curves and good deceleration data are available.

The instrumentation and data are described in Section 2. The fragmentation model used to reveal meteoroid fragmentation behavior from fireball data is presented in Section 3. The modeling results are given in Section 4 separately for the confirmed meteorite falls and the additional fireballs. For the latter, orbital data and coordinates of the strewn fields are also provided. For the confirmed falls, these data can be found in the original papers. The revealed fragmentation behavior and its implication for the structure of ordinary chondritic meteoroids is discussed in Section 5 and summarized in Section 6.

2. Instrumentation and Data

The data analyzed here were primarily obtained in the scope of the European Fireball Network (EN), a long-term project of observing fireballs over central Europe (Spurný et al. 2007), in 2009–2018. During that period, the main instrument of the network changed from the older Autonomous Fireball Observatory (AFO; described in Spurný et al. 2007) to the modern Digital Autonomous Fireball Observatory (DAFO; described briefly in Spurný et al. 2017b). The purpose of both types of instruments was to take images of the whole sky during each night when the sky was at least partly clear. The main difference is that AFO used photographic film and usually took one exposure per night, while DAFO uses two digital DSLR Canon 6D cameras and is taking multiple exposures 35 s long. To enable the measurement of fireball velocities, AFO employed a mechanical rotating shutter placed in front of the film. DAFO uses an LCD shutter placed behind the lens. The shutter break frequency is similar in both cases, 15 Hz for AFO and 16 Hz for DAFO.

Besides avoiding the laborious manipulation with photographic film, the advantages of DAFO are higher sensitivity and better performance in difficult conditions (moonlit nights, partly cloudy nights, and twilight periods). The pointlike appearance of stars and the higher number of stars in DAFO images (especially in regions close to the horizon) make the astrometric reduction easier and more reliable. The disadvantage of DAFO is a lower dynamic range, which makes the photometry of bright fireballs difficult. Nevertheless, the main photometric instrument is the radiometer, which is part of both AFO and DAFO.

The radiometer is a photomultiplier tube with a flat entry aperture without any optics, directed to zenith. It takes the measurement of the total brightness of the sky 5000 times per second. The dynamic range is 20 bits, providing information about the luminosity of fireballs in linear scale for fireballs of apparent magnitudes from about −2 to about −17. Fireballs brighter than −17 mag (i.e., superbolides) can be reliably measured from more distant stations, where their apparent magnitude is lower. The radiometer provides intensity in relative units, and the zero-point must be determined for each fireball using photographic data (which provide absolute fireball photometry by comparison with stars). For this purpose, the nonsaturated part of the photographic data is used (usually the part of the light curve when the fireball magnitude was between −5 and −8). The response of the radiometer as a function of zenith angle was measured in the laboratory. To join the radiometric and photographic data easily together, a time mark is produced by the DAFO LCD shutter every second by skipping one interruption (i.e., making one dash on the fireball image three times longer). Both the LCD and radiometer time are controlled by the GPS signal to keep the absolute time correct with submillisecond precision. In the case of AFO, visible features on the photographic light curve had to be compared with the radiometric curve to determine absolute timing.

The DAFOs started to be deployed at the stations of the network at the end of 2013. By the end of 2014, all stations in the Czech Republic were equipped with DAFOs. DAFOs and AFOs were then run in parallel for the next few years (depending on station). In addition, several new DAFO stations were build in 2015–2018. By the end of 2018, only DAFOs were used at all 14 EN stations in the Czech Republic, three in Slovakia, and one in Austria. Old-type mirror cameras (Oberst et al. 1998) were used in Germany as part of the EN.

2.1. Observed Meteorite Falls

One of the purposes of the EN is to observe meteorite-dropping fireballs. The data are used to predict the location of meteorites, study the interaction of the meteoroid with the atmosphere, and compute the pre-encounter heliocentric orbit. Recovering the meteorites, however, is not easy. While the

Table 1
Meteorite Falls Analyzed in This Study

Name	Type	Date	Latitude (°N)	Longitude (°E)	Country	Entry Mass from Model (kg)	Recovered Mass (kg)	No. of Fragments	References
Jesenice	L6	2009 Apr 9	46.421	14.052	Slovenia	250	3.61	3	(1), (2)
Košice	H5	2010 Feb 28	48.757	21.160	Slovakia	4000	11.3	218	(3), (4)
Križevci	H6	2011 Feb 4	46.039	16.590	Croatia	53	0.29	1	(5)
Žďár nad Sázavou	L3.9	2014 Dec 9	49.508	15.963	Czech R.	150	0.087	3	(6), (7)
Stubenberg	LL6	2016 Mar 6	48.306	13.093	Germany	450	1.47	6	(8), (9), (P)
Hradec Králové	LL5	2016 May 17	50.301	15.728	Czech R.	90	0.13	1	(P)
Renchen	L5-6	2018 Jul 10	48.610	7.948	Germany	17	1.23	6	(10), (P)

References. (1) Spurný et al. (2010), (2) Bischoff et al. (2011), (3) Borovička et al. (2013b), (4) Tóth et al. (2015), (5) Borovička et al. (2015), (6) Spurný et al. (2020), (7) Kalasová et al. (2020), (8) Spurný et al. (2016), (9) Bischoff et al. (2017), (10) Bischoff et al. (2019), (P) papers in preparation.

location of the fireball luminous trajectory can be determined with a precision of the order of tens of m, the dark flight (usually starting from heights between 20 and 30 km) cannot be observed, and the final meteorite location depends on the exact meteorite mass and shape, as well as upper atmosphere winds. Taking winds from meteorological models and assuming a spherical shape of the meteorite, the location can be computed as a function of meteorite mass (more exactly, a parameter combining mass and density). In the case of good dynamic data toward the end of the luminous trajectory, meteorite mass can be estimated from the observed speed and deceleration. A fragmentation model (Section 3) can provide a likely mass range for additional smaller meteorites, and the whole strewn field can be modeled. Depending on the geometry (especially the slope of the trajectory), meteoroid fragmentation heights, wind speeds and directions, and meteorite mass range, strewn fields can have various sizes and shapes. Typically, the area of the highest probability to be searched is a strip of a couple hundred m wide and several to tens of km long. The uncertainty in the position of the largest fragment is typically a few hundred m. Finding a single stone in the European landscape is a challenge. The experience shows that the more favorable cases are those producing a large number of small meteorites. There is a chance to find at least some of them.

The EN cameras have so far obtained data for 12 recovered meteorites (from about 30 meteorites with known trajectories worldwide), and 10 of them are ordinary chondrites. Radiometric light curves are available for eight of them, but in the case of the Ejby meteorite fall in Denmark (Spurný et al. 2017a), the quality of the light curve is not sufficient for fragmentation modeling due to the large distance of the camera from the fireball. Seven meteorite falls were therefore modeled. They are listed in Table 1. The meteorite name, classification, date of fall, coordinates of the largest recovered fragment, entry mass estimated from the fragmentation modeling (Section 4.1), total recovered mass, and number of recovered fragments are given.

The Jesenice and Križevci meteorite falls occurred relatively far from the EN cameras, but the radiometric curves are good. The EN cameras were combined in these cases with Slovenian and Croatian cameras for as complete a description of the fireballs as possible (Spurný et al. 2010; Borovička et al. 2015). For Jesenice, there are no deceleration data, but the trajectory, entry speed, and light curve could be determined well. The first Jesenice meteorite was found casually before the exact fireball trajectory was computed. The Križevci meteorite was found by a Croatian group on the basis of a preliminary trajectory computed from Croatian cameras.

Table 2
Basic Parameters of Trajectories of Meteorite Falls

Name	Begin. Height (km)	End Height (km)	Zenith Angle (deg)	Entry Speed (km s^{-1})	Maximum Magnitude
Jesenice	88	~18[a]	31	13.78	−15
Košice	N/O[b]	17.4	30.2	15.0	−18
Križevci	98.10	21.81	24.6	18.21	−13.7
Žďár n. S.	98.06	24.71	64.8	21.89	−15.3
Stubenberg	85.92	17.19	19.6	13.91	−15.4
Hradec K.	74.34	23.54	42.5	13.31	−11.5
Renchen	80.40	18.47	11.9	18.62	−13.4

Notes.
[a] Fireball end not directly observed. End height estimated from the light curve.
[b] Fireball beginning not observed. Fireball entered the field of view at a height of 68.3 km.

The Košice meteorite fall occurred in bad weather when all EN cameras were clouded out. The trajectory, velocity, and deceleration were determined from three casual video records extracted from security cameras in Hungary (Borovička et al. 2013b). Of course, the precision is lower than from dedicated cameras. But one video shows a fragment following the main body toward the end. Thanks to the extreme brightness of this superbolide, good radiometric curves were obtained by EN cameras through thick clouds (in full Moon night!).

The last four meteorites were recovered on the basis of observations by EN cameras. Žďár nad Sázavou fell in the middle of the network and has excellent data. Stubenberg and Hradec Králové were affected by bad weather. On some stations, only parts of the fireballs were recorded between clouds. The same is valid for Renchen, where, moreover, the dynamics was measurable only on a German camera with lower resolution. In all cases, nevertheless, the trajectory, orbit, and light curve were determined reliably. The only missing data are decelerations at the end of the trajectories. The basic parameters of the trajectories are given in Table 2.

2.2. Additional Fireballs

To enlarge the statistics, the analysis of seven meteorite falls was supplemented by the analysis of 14 other fireballs, which almost certainly also dropped meteorites (at least small ones with masses of the order of tens of g), but the meteorites were

Table 3
Trajectories of Fireballs Analyzed in This Study

Name (Date)	Time UT (hms)	Beginning Point			End Point			Zenith Angle (deg)	Entry Speed (km s^{-1})	Maximum Magnitude
		Longitude (°E)	Latitude (°N)	Height (km)	Longitude (°E)	Latitude (°N)	Height (km)			
2015 Jun 2	215119	12.0153	49.8729	85.09	11.9737	50.0746	24.30	20.4	16.28	−9.7
2015 Aug 26	233145	11.8268	48.3390	90.04	12.3564	48.9995	28.43	53.3	19.36	−11.5
2016 Nov 10	022429	20.6512	48.6528	91.86	21.0221	48.3100	20.37	33.3	23.49	−12.5
2016 Dec 7	041110	13.5418	49.7472	86.70	15.0116	49.7543	28.64	61.3	21.03	−10.3
2017 Feb 24	190640	14.0102	48.3757	84.22	13.3198	48.5257	31.38	45.6	17.82	−9.6
2017 Feb 27	023122	13.4461	49.1474	95.44	14.2898	49.6462	27.95	50.9	31.24	−12.4
2017 Nov 14	164658	11.0091	50.0767	94.71	07.4990	50.2612	26.17	74.3	19.77	−12.8
2017 Dec 3	171520	14.6954	49.2097	77.89	14.4618	49.0219	21.18	25.4	13.32	−9.4
2018 Jan 18	182623	14.6084	49.8803	87.62	14.3817	49.3879	26.39	43.2	20.06	−10.2
2018 Apr 8	184736	17.5960	46.9418	88.65	16.6598	46.1782	25.05	59.6	16.45	−12.7
2018 May 23	194647	17.0983	49.9734	80.37	17.1427	49.5864	23.47	37.3	12.92	−9.4
2018 Sep 11	214648	15.6510	47.0533	91.43	15.6134	47.3531	25.92	27.2	23.65	−14.0
2018 Oct 8	195513	14.4817	50.0272	82.05	14.2281	50.3284	23.51	33.3	13.98	−9.1
2018 Nov 29	041019	16.5184	46.6258	90.73	16.5928	45.9443	22.45	48.1	25.82	−12.5

not recovered. All of these fireballs were observed very well, including dynamic data along the whole trajectory. All of them are of type I, according to the classification of Ceplecha & McCrosky (1976), and were therefore produced by stony meteoroids, most probably ordinary chondrites. We cannot exclude the presence of enstatite chondrites or some strong achondrites, but the presence of carbonaceous chondrites, which typically belong to type II, is unlikely, and irons, which belong to type III (Vojáček et al. 2020), can be excluded. On a statistical basis, 13 of the 14 type I fireballs should be ordinary chondrites, since from ordinary and enstatite chondrites and achondrites, ordinary chondrites form 93% of meteorite falls.

The list of fireballs is given in Table 3. The fireballs will be referred to according to their date of appearance. The listed time is valid for the fireball beginning. The official code of the fireball can be constructed from the date and time in the form ENddmmyy_hhmmss, e.g., EN020615_215119 for the first one. The geographical coordinates of the observed beginning and end points take into account Earth curvature and the estimated curvature of the trajectory due to gravity. The zenith angle, i.e., zenith distance of the radiant (0° means vertical trajectory; 90° means horizontal flight), is valid for an average point along the trajectory. Finally, the speed at the top of the atmosphere and the maximum absolute (i.e., at the distance of 100 km) stellar magnitude are given.

The fireball data are mainly based on observations by DAFOs. In seven cases, supplementary video cameras installed at two EN stations (Ondřejov and Kunžak) in 2016–2018 were also used. These are Dahua surveillance cameras and provide 20 frames s^{-1} in resolution 2688 × 1520 pixels with a field of view of 56° × 32°. In the final configuration, 13 cameras are continuously working at each station. Video cameras provided additional valuable dynamic data, especially for fireball 2017 November 14, where the dynamics was fully based on video data because of too-slow angular motion at all DAFO stations, which made the shutter breaks hardly measurable. In three other cases (2017 December 3, 2018 April 8, and 2018 May 23), video data contained fragments following the main bodies (invisible on long-exposure DAFO photographs). The fragments can be visible in even more detail on the Fireball Intelligent Positioning System (FIPS) cameras installed in Ondřejov and Kunžak. The cameras, with a field of view of about 15° on a moving mount, are tracking fireballs according to a navigation all-sky video. The FIPS captured six fireballs at least partly and showed separated fragments in four of them (2017 December 3, 2018 April 8, 2018 September 11, and 2018 October 8). Fragment positions could not be calibrated, but their presence qualitatively confirmed the results from other cameras and the modeling.

Additional data outside the EN were used in some cases. An amateur video was used for the 2018 May 23 fireball. One video camera of the Croatian Meteor Network was used for both 2018 April 8 and 2018 November 29 (in both cases, the video showed the very end of the fireball). Amateur still photographs were used to improve the trajectory solution for 2017 November 14, 2018 April 8, and 2018 May 23.

Spectra were obtained for 11 fireballs (all except the first three in Table 3) by either a spectral DAFO or a supplementary video camera (see Borovička et al. 2019c, for the description of the EN spectral program). The spectra have not yet been analyzed qualitatively but are consistent with chondritic compositions of the meteoroids. The usual lines of Na, Mg, and Fe dominate the spectra.

Meteorite searches were performed in all 14 cases. Some of them were rather brief, and some of them were intensive, depending on the conditions in the strewn field. No meteorites were found.

3. The Semiempirical Fragmentation Model

3.1. Description of the Model

The fragmentation model used to fit the observed data was first developed for the analysis of the Košice meteorite fall (Borovička et al. 2013b). It has also been described in the review by Popova et al. (2019). A more detailed description is given here. We call the model semiempirical because the locations of fragmentation points must be determined from empirical data for each modeled fireball.

The model assumes a finite number of fragments, which move independently. At any time, the total luminosity of the fireball is the sum of the luminosities of all individual fragments. The basic physical theory of meteors (Ceplecha et al. 1998) is used to compute the motion, ablation, and radiation of fragments. The fragment luminosity is proportional

to the loss of kinetic energy,

$$I = -\tau(v, m)\left(\frac{v^2}{2}\frac{dm}{dt} + mv\frac{dv}{dt}\right), \quad (2)$$

where τ is the luminous efficiency (dimensionless), v is the velocity, m is the mass of the fragment, and t is time. The luminosity I can be considered in either the whole spectral range or a limited range (e.g., visual). The luminous efficiency must be adjusted accordingly. In this paper, we consider the whole spectral range. The luminous efficiency is assumed to depend on velocity and mass. We used the velocity dependence found by Pecina & Ceplecha (1983) and confirmed by ReVelle & Ceplecha (2001). The mass dependency was adapted from ReVelle & Ceplecha (2001) so that the shape of the function is the same but the luminous efficiency for small meteoroids is not as low as assumed by ReVelle & Ceplecha (2001). We believe that the luminous efficiency may be low (of the order of 0.1%) for small meteoroids observed with television techniques high in the atmosphere, but for small fragments separated from bigger meteoroids lower in the atmosphere, we found that values of about 2.5% at 15 km s^{-1} are needed. For large meteoroids ($\gg$1 kg), 5% at 15 km s^{-1} was used. The full expression for luminous efficiency τ (in percent) is

$$\ln\tau = 0.567 - 10.307\ln v + 9.781(\ln v)^2 - 3.0414(\ln v) + 0.3213(\ln v)^4 + 0.347\tanh(0.38\ln m) \quad \text{for} \quad v < 25.372, \quad (3)$$

$$\ln\tau = -1.4286 + \ln v + 0.347\tanh(0.38\ln m) \quad \text{for} \quad v \geqslant 25.372, \quad (4)$$

where v is in km s^{-1} and m is in kg (ln is natural logarithm and tanh is hyperbolic tangens). The dependency is presented in graphical form in Figure 1.

Since τ is dimensionless, the intensity I in Equation (2) is in energetic units. To compare it with observations, I must be converted to absolute magnitudes, M, by

$$M = -2.5\log(I/1500), \quad (5)$$

where I is in watts. The equation follows from the estimate that, for the usual meteor plasma temperature of 4500 K, a zero magnitude meteor radiates 1500 W into the whole spectral range (Ceplecha et al. 1998).

Meteoroid deceleration and ablation are given by the drag and ablation equations, respectively:

$$\frac{dv}{dt} = -\Gamma A\delta^{-2/3}\rho m^{-1/3}v^2, \quad (6)$$

$$\frac{dm}{dt} = -\Gamma A\delta^{-2/3}\sigma\rho m^{2/3}v^3, \quad (7)$$

where Γ is the drag coefficient ($0 < \Gamma \leqslant 2$), A is the shape coefficient ($A = SV^{-2/3}$, where S is the head cross section and V is volume; note that for sphere $A = 1.21$), δ is the meteoroid bulk density, ρ is the atmospheric density (a function of atmospheric height), and σ is the ablation coefficient. Ceplecha et al. (1998) presented an integral solution of these equations based on the work of Pecina & Ceplecha (1983). The solution assumes that the product $\Gamma A\delta^{-2/3}$ and the ablation coefficient σ are constant. The fireball trajectory is assumed to be linear, but the Earth's curvature is taken into account. The relation between the length along the trajectory and atmospheric height is therefore quadratic.

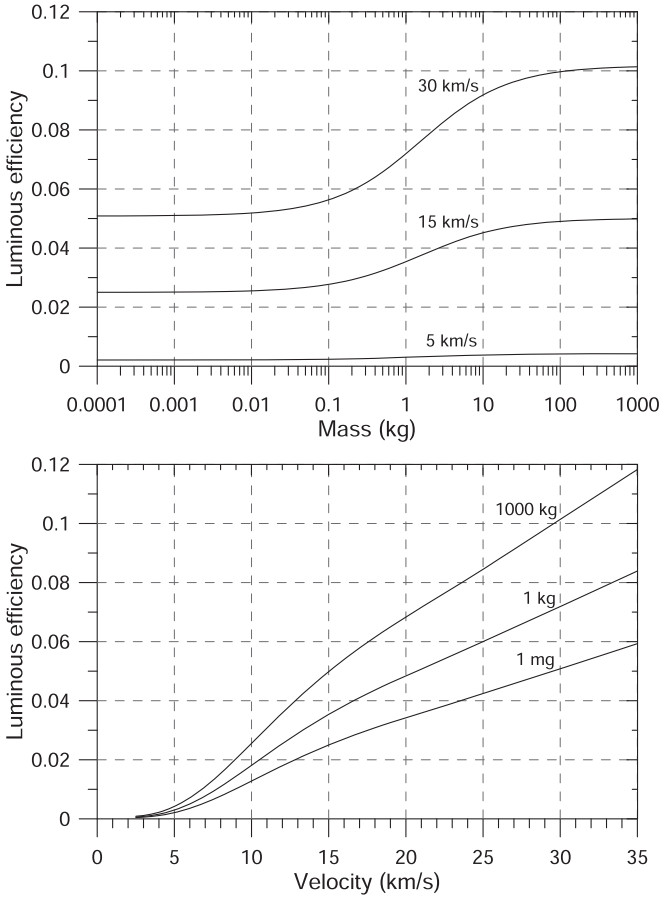

Figure 1. Assumed luminous efficiency as a function of meteoroid mass and velocity.

The integral solution makes it possible to analytically compute the position, velocity, mass, and luminosity of each fragment as a function of time. The input values are the height, velocity, and mass at the initial time; the known trajectory; and the constant parameters ΓA, δ, and σ. Atmospheric densities are taken from the NRLMSISE-00 model (Picone et al. 2002). The computation proceeds until the next fragmentation point or until the velocity decreases to 2.5 km s^{-1}, when the ablation and radiation are supposed to cease.

The model considers individual fragments, multiple fragments, and dust. Fragments are formed in gross-fragmentation events. Dust can be released either suddenly or by erosion. Multiple fragments are simply identical fragments (of the same mass and all other parameters) formed at the same time. The computation is then performed only once, and the resulting luminosity is multiplied by the number of fragments. Of course, this is an idealization intended to save computation time. Similarly, dust is a large number of usually small fragments (dust particles) in a given mass range. The masses of dust particles are sorted into mass bins. The number of mass bins per order of magnitude of mass, b, can be chosen. For example, if $b = 4$, the logarithms of masses are separated by 0.25. The parameters of the dust are the total mass, D; the upper and lower mass limits of dust particles, m_0 and m_k, respectively; and

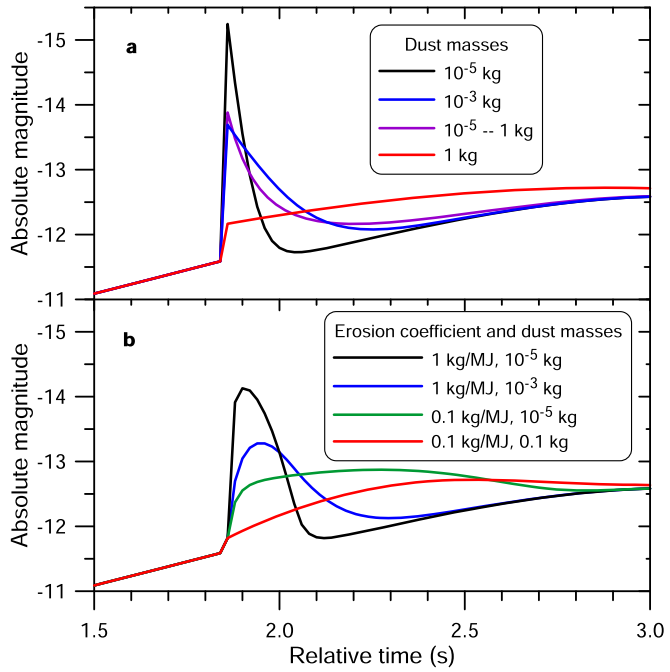

Figure 2. Effects of single fragmentation events with various parameters on the shape of the light curve. Sudden releases of dust or multiple fragments (a) and formation of an erosion fragment (b) are shown. In all cases, a 100 kg meteoroid moving at 15 km s^{-1} at a height of 40 km loses 25 kg of mass. The other parameters are $\Gamma A = 0.8$, $\delta = 3400$ kg m^{-3}, $\sigma = 0.005$ kg MJ^{-1} for all fragments and dust particles, $s = 2$, and trajectory slope 45°. Computations are done with a time resolution of 0.02 s.

the mass distribution index, s. A power-law mass distribution is assumed. The number of particles in the ith bin with masses m_i is

$$n_i = n_0 \left(\frac{m_0}{m_i} \right)^{s-1}, \quad (i = 0, 1, \ldots, k), \tag{8}$$

where k is the number of additional mass bins (i.e., other than the bin containing the particles of the largest mass),

$$k = b \log(m_0/m_k), \tag{9}$$

and

$$m_i = m_0\, 10^{-i/b}, \quad (i = 0, 1, \ldots, k). \tag{10}$$

The number of particles of the largest mass is

$$n_0 = \frac{D}{(k+1)m_0}, \quad \text{for} \quad s = 2, \tag{11}$$

or

$$n_0 = \frac{D}{m_0} \cdot \frac{1 - p^{(2-s)}}{1 - p^{(k+1)(2-s)}}, \quad \text{for} \quad s \neq 2, \tag{12}$$

where $p = 10^{-1/b}$. Since n_i and k are integer numbers, integer parts are taken in Equations (8), (9), (11), and (12).

The effects of a sudden dust release on the light curve are shown in Figure 2(a). The release of small dust particles produces a short bright spike. Larger dust particles produce longer and asymmetric peaks with quick rise and slower decay. The formation of multiple large fragments produces a step on the light curve.

To be able to reproduce more symmetric peaks and the long humps often observed on real light curves, the concept of eroding fragments was introduced. The erosion formalism is the same as that formulated for faint Draconid meteors by Borovička et al. (2007). The concept of quasi-continuous detachment of small particles was, nevertheless, formulated much earlier (e.g., Simonenko 1973). In our approach, the eroding fragment is losing mass by ablation described by Equation (7) and erosion described by an analogical equation where the ablation coefficient σ is replaced by the erosion coefficient η. Both coefficients have the same unit, kg MJ^{-1}, or, equivalently, s^2 km^{-2}. The ablated mass is in vapor form and immediately contributes to fireball radiation. The eroded mass is released in the form of dust particles, which only subsequently ablate and radiate. The dust parameters are m_0, m_k, and s, as in the case of immediately released dust. The dust mass distribution is computed from Equations (8)–(12), where the total dust mass D is replaced by the mass eroded within the time step of computation.

The light-curve effects produced by eroding fragments are illustrated in Figure 2(b) for four combinations of the erosion coefficient η and the mass of dust particles. In these examples, all dust particles were supposed to have the same mass. The erosion continued until the eroding fragment was completely exhausted. The model formalism allowed the erosion to stop (and continue only ablation) after a prescribed part of the fragment was eroded out, but this feature was not used in modeling the fireballs presented here. Also, the eroding fragments were not subject to further gross-fragmentation events. Individual and multiple fragments, on the other hand, could fragment repeatedly. Dust particles, released either suddenly or by erosion, cannot be subject to fragmentation in this model.

3.2. Modeling Procedure

The model was used to fit the observed fireball light curves and dynamics, i.e., length along the trajectory as a function of time. The trajectory was always known from a multistation linear least-squares solution (Borovička 1990). A point at the trajectory near the observed fireball beginning was chosen as the starting point. Here the meteoroid was assumed to be a single body described by its mass, density, velocity, drag, shape, and ablation coefficients. The velocity was tuned to fit the observed dynamics at the beginning of the fireball. The first guess of the mass was obtained from the total radiated energy, taking into account the velocity and the approximate luminous efficiency for that velocity. Nevertheless, the initial mass had to be adjusted when the modeling proceeded. The density of corresponding meteorites was used for meteoroid density. If no meteorite was recovered, a value of 3400 kg m^{-3} was assumed. For other parameters, the canonical values were $\Gamma A = 0.8$ and $\sigma = 0.005$ kg MJ^{-1}. In order to keep the number of free parameters of the model at a minimum, these parameters and the density were also used, if possible, for all subsequent fragments and dust particles. Such a uniform approach to all fireballs was preferred to avoid introducing biases when studying meteoroid fragmentation behavior, which was the main goal of this work.

The modeling was done manually by a trial-and-error method. Fragmentation points were identified according to features on the light curve (flares, sudden changes in slope). Another sign of fragmentation can be a sudden increase of deceleration. In a few cases, the fragmentation point was identified according to a change of trajectory, i.e., a change of

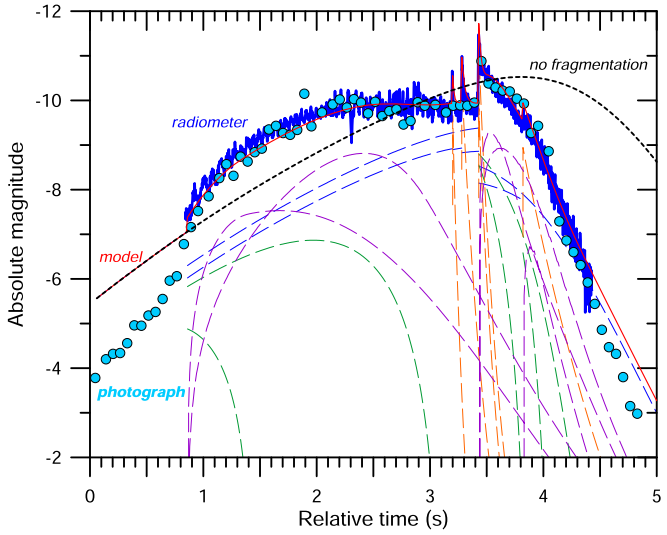

Figure 3. Observed and modeled light curve of fireball 2015 August 26. The radiometric light curve (blue line) and photographic data (light blue dots) are shown from only one station for clarity. The modeled light curve is shown as a solid red line. The contributors to the light curve are shown as dashed lines: blue for regular fragments, green for eroding fragments, orange for immediately released dust, and violet for dust from eroding fragments. The light curve modeled without any fragmentation is shown as a dotted black line for comparison.

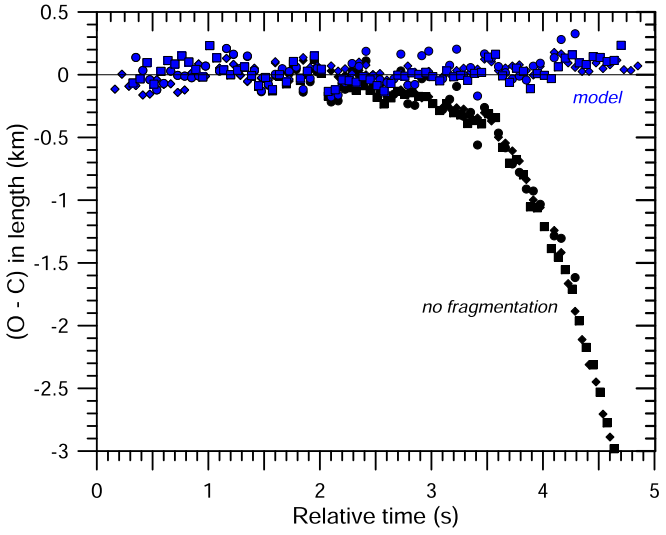

Figure 4. Dynamics of fireball 2015 August 26. The difference between the observed and modeled length along the trajectory is shown as a function of time. Black symbols are for the model without fragmentation; blue symbols are for the fragmentation model. The small positive trend of the blue symbols at the end was allowed to account for gravity acceleration, which was not modeled directly. Different symbols correspond to observations from different stations.

the direction of flight (by 1°–2°), before the end of the fireball. The change was supposed to be produced by a lateral impulse acquired during breakup. Since there was no flare and no big change of deceleration in the observed cases, the fragmentation was modeled by a loss of a relatively small amount of mass in the form of a few fragments. Such cases demonstrate that there may be some fragmentation events that are not apparent in the light curve or dynamic data and can remain unnoticed if there is no sufficiently large lateral impulse or geometric data are not precise enough. On the other hand, these were only minor events with minor mass loss.

As an example, light-curve modeling is shown in Figure 3 for fireball 2015 August 26. The initial meteoroid mass was found to be 6.5 kg. At the beginning, the modeled brightness was higher than observed, since the model assumes a steady-state ablation, while in reality, the ablation started gradually. At a time of ≈0.8 s, the brightness started to increase rapidly. A hump was formed on the light curve lasting for 2 s (time 1–3 s). The brightness was elevated above the level expected for a single nonfragmenting body. This feature could be modeled by a disruption of the 6.5 kg meteoroid into two regular (2.6 and 1.5 kg) and two eroding (1.9 and 0.5 kg) fragments at a time of 0.9 s (height 69 km, dynamic pressure 0.04 MPa). The ablating dust released gradually from the eroding fragments formed the hump. In fact, each "dust" particle was assumed to have mass of 1 g here. The erosion coefficients of the two eroding fragments were 0.1 and 1 kg MJ^{-1}, respectively. Of course, these parameters are only schematic. The substantial fact is the identification of the fragmentation at a height of 69 km and the fact that the following 2 s of the flight could be fitted without further disruption (erosion is considered here as a thermal process analogous to ablation, not as a "real" fragmentation). Note that there are semiregular oscillations visible on the radiometric light curve (confirmed on several independent radiometers) that are not attributed to fragmentation. It might be a demonstration of an instability process in ablation.

The initial fragmentation at 0.9 s can also be confirmed from fireball dynamics. Dynamics also enabled us to determine the mass of the largest fragment after the fragmentation. The observed length along the trajectory deviates from that expected for a nonfragmenting body already at time 2.5 s (Figure 4). The dynamics between 0.9 and 3.4 s corresponds to a fragment of initial mass 2.6 kg, decreasing during that interval to 2.1 kg due to ablation. The masses of other modeled fragments were estimated from the light-curve fit. Unless there is a video record showing more fragments, dynamic data are available only for the leading (foremost) body. Note that the leading bodies can exchange, as was directly observed in videos of the Morávka (Borovička & Kalenda 2003) and Chelyabinsk (Borovička et al. 2013a) superbolides.

After more than 2 s of quiescence, the 2015 August 26 fireball showed three short flares at 3.2, 3.3, and 3.4 s (heights 43–40.5 km, dynamic pressures 0.9–1.15 MPa). After the third flare (the largest one), the brightness remained elevated for about 0.3 s and then decreased rapidly, especially after another, smaller flare at 3.8 s (37 km, 1.4 MPa). The flares at 3.2 and 3.3 s were modeled as immediate dust releases of particles of 10^{-5}–10^{-6} kg (millimeter-sized). For the flare at 3.4 s, two eroding fragments were added. The eroded dust formed the bulk of the radiation at 3.5–3.8 s. The particle masses were 10^{-4} −0.05 kg (centimeter-sized); the erosion coefficients were 0.05–0.1 kg MJ^{-1}. Similar erosion parameters were used for the last flare at 3.8 s, where no millimeter-sized dust was released.

The fragmentation sequence, i.e., which fragment fragmented at which time, cannot be revealed unambiguously. But the quick increase of deceleration in comparison with the no-fragmentation case at time 3.5 s (Figure 4) shows that the mass of the leading fragment decreased significantly. To model the dynamics and light curve, it was assumed that two 0.5 kg fragments emerged after the main fragmentation at 3.4 s. One of them was destroyed at 3.8 s. For the second fragment, no further fragmentation was needed to fit the dynamics, but the ablation coefficient had to be enhanced to 0.01 kg MJ^{-1} from

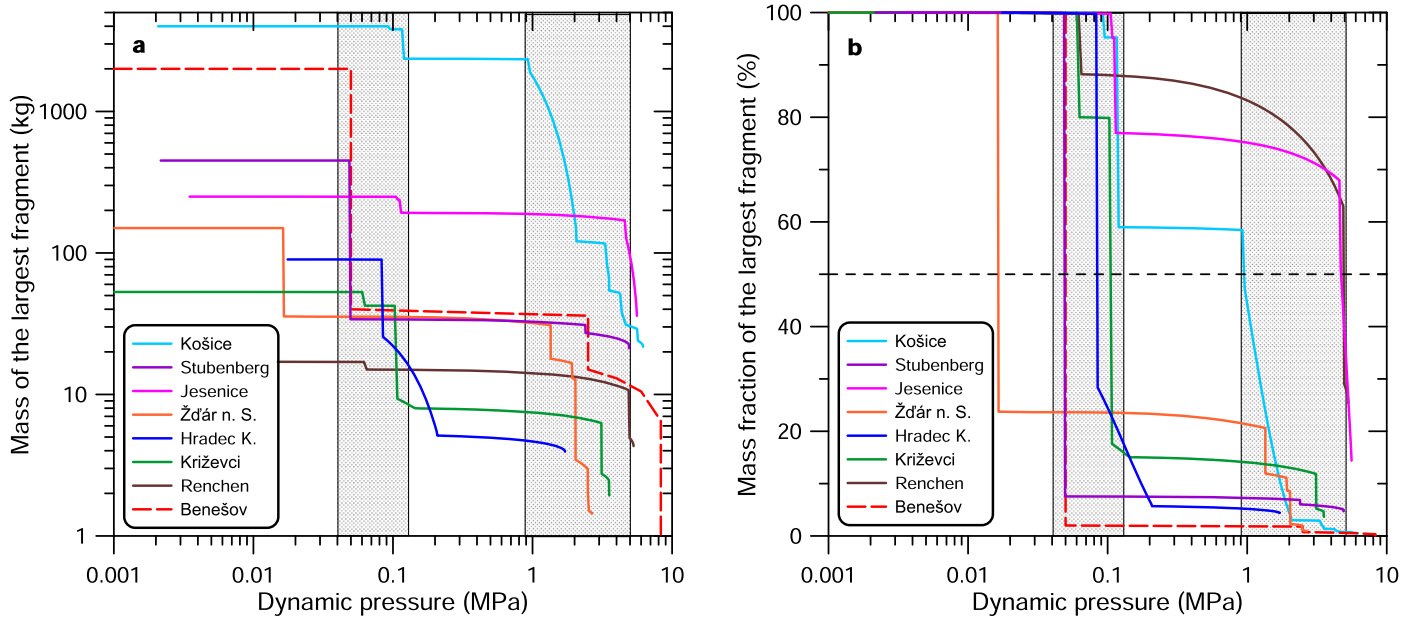

Figure 5. Modeled mass of the largest surviving fragment as a function of increasing dynamic pressure for seven meteorite falls. Absolute mass values are plotted in panel (a); percentages of the initial mass are plotted in panel (b). The result of an approximate analysis of the Benešov meteorite fall of 1991 May 7 (Borovička 2016) is included for comparison. The fragmentations preferentially occurred in two dotted intervals of dynamic pressures. One exception was the early fragmentation of Žďár nad Sázavou.

the nominal value of 0.005 kg MJ^{-1}. The mass of this fragment (0.5 kg when formed and 0.12 kg at the end) was determined from the dynamics. In addition to this single meteorite, some meteorites smaller than 0.03 kg could result from the largest bodies modeled as dust. The modeled brightness toward the end of the fireball was somewhat higher than observed (Figure 3). This discrepancy could be removed either by decreasing the luminous efficiency at speeds below 10 km s^{-1} or by simultaneously lowering both the mass and ΓA of the fragment.

The example of the 2015 August 26 fireball demonstrates the interplay between light curve and dynamics. The positions of the important fragmentation points can be determined robustly from the light curve. The initial mass of the meteoroid and the amount of mass released as dust is also determined from the light curve (and known velocity). The masses of leading fragments can be determined from fireball dynamics, i.e., observed deceleration. Other fragments can be studied directly only if they were imaged on a video. Otherwise, the evidence of their existence is obtained only indirectly from their contributions to the light curve, and the adopted solution (number and masses of fragments) is usually not unique. Unless some fragments are well observed from two (or more) well-separated stations, all fragments are assumed to follow the same trajectory as the main body. Of course, all derived masses depend on the assumed values of luminous efficiency, fragment density, shape, etc. Masses are therefore less certain than dynamic pressures at fragmentations.

4. Results

The procedures explained in Section 3 were applied to the observations of verified and suspected meteorite falls described in Section 2. The results are presented separately here for both groups.

4.1. Meteorite Falls

In Figure 5(a), the results of fragmentation modeling of seven meteorite falls from Table 1 are presented. The approximate analysis of the Benšov meteorite fall from Borovička (2016) is added for comparison. Note that the models for Jesenice and Križevci were slightly revised in comparison with original publications. For Jesenice, the fragmentation at the height of 46 km was omitted because it was based on seismic data, which are not very reliable for these heights, and there is no sign of fragmentation at this height in the light curve. The light curve suggests an earlier fragmentation at about 55 km.

The mass of the largest surviving fragment is plotted as a function of dynamic pressure. Dynamic pressure always increases along the trajectory as the meteoroid penetrates into denser atmospheric layers. Only when the meteoroid is decelerated significantly toward the end of the luminous trajectory does the dynamic pressure start to decrease. The part of the trajectory with decreasing pressure is not plotted. Although the fragmentation can continue here and also during the dark flight, as is evidenced by the incomplete fusion crust of some meteorites (e.g., Borovička & Kalenda 2003; Bischoff et al. 2019), the reason is not increasing dynamic pressure. It is probably the aftermath of previous fragmentations.

Figure 5(a) shows stepwise decreases of masses due to gross fragmentations, gradual but steep decreases due to erosion (e.g., for Hradec Králové), and only slight decreases due to ablation. If the erosion decrease was followed by a much slower decrease, it does not mean that the erosion stopped at that point. It means that the mass of the eroding fragment decreased below the mass of a regular fragment, which then became the largest surviving fragment.

It is obvious from Figure 5(a) that the gross fragmentations did not occur randomly. We can clearly see two phases of fragmentations. The first phase typically occurred between 0.04 and 0.12 MPa. Only Žďár nad Sázavou had already fragmented

at 0.017 MPa. The second phase of fragmentation occurred at 1–5 MPa (for Košice at 0.96–5.7 MPa). No gross-fragmentation events occurred in these seven fireballs at intermediate dynamic pressures of 0.12–0.96 MPa.

Figure 5(b) shows the same data, but the mass of the largest fragment is normalized to the initial meteoroid mass. In four of the seven cases, the first phase of fragmentation can be considered as catastrophic. Disruption was defined as catastrophic (in the context of tidal disruption of asteroids) when the largest surviving fragment contained less than 50% of the original mass (Richardson et al. 1998). For Košice, the first phase was also almost catastrophic, with a surviving fragment mass of about 60% of the original mass. In fact, the mass of the surviving fragment is not well restricted by the data in this case. Replacing the ≈2400 kg fragment in the model with two pieces of half-mass would also be consistent with observations. So, only Renchen and Jesenice were surely not catastrophically disrupted in the first phase. They lost less than 25% of their mass there. Both of these meteoroids were also most resistant in the second stage of fragmentation. They were disrupted only at about 5 MPa.

The second stage of fragmentation was severe in most cases. Only Hradec Králové, which was disrupted into relatively large fragments during the first phase and the subsequent erosion process, showed no significant fragmentation above 1 MPa, at least judging from the light curve. There are no dynamic data at the end of the trajectory. The fact that the recovered meteorite shows only a thin fusion crust on part of the surface, nevertheless, demonstrates that there was a late-stage fragmentation (Gattacceca 2019).

Figure 5 shows only the fragmentations that occurred for the largest fragment at a given time. We therefore present in the histograms in Figures 6(a) and (b) all gross-fragmentation events in all seven meteorite falls. Panel (a) simply shows the number of events in each interval of dynamic pressures. In panel (b), each fragmentation event is weighted by the relative mass loss. Mass loss is defined here as the difference between the mass before fragmentation and the mass of the largest regular (i.e., noneroding) fragment after the fragmentation. Relative mass loss is defined as the mass loss divided by the initial mass of the whole meteoroid at the atmospheric entry.

The dichotomy of fragmentation strengths is clearly visible in Figures 6(a) and (b). Most of the mass was lost in the first phase of fragmentation at pressures up to 0.1 MPa. The fragmentations in the second phase were more numerous but involved less mass. The reason was that the first phase usually produced a number of small fragments, which then disrupted in the second phase, but the mass loss was small in each case. Some fragments lost mass repeatedly in small amounts during the second phase. Only Jesenice and Renchen lost the most mass during the second phase. There was no case with negligible fragmentation so that most mass would be lost just by ablation. In that case, the meteorite could contain a significant part of the initial mass. Such cases exists but are rare. One example was the Carancas crater-forming event (Borovička & Spurný 2008; Brown et al. 2008).

4.2. Fireballs

The results of analysis of meteorite-dropping fireballs with unrecovered meteorites are presented in Figures 6(c) and (d) and Figure 7. Except for two cases, these fireballs were produced by small meteoroids of masses not exceeding 20 kg. Smaller mass is, in fact, an advantage for studying the outcome of the first phase of fragmentation. Since smaller meteoroids already show deceleration at middle heights corresponding to dynamic pressures of tenths of MPa, it is possible to compute the mass of the largest fragment at these heights from dynamics.

Figures 6(c) and (d) show that the bimodality of strengths is present in these fireballs as well, though in contrast to cases with recovered meteorites, fragmentation events were also observed at pressures of 0.1–1 MPa. There were only a few minor fragmentations at 0.12–0.3 MPa. More significant events occurred at 0.3–1 MPa. Figure 7 shows that major fragmentations of the leading fragments occurred at these pressures in four fireballs. Two of them are the two smallest meteoroids in our sample, 2018 January 18 and 2017 February 24, both with a mass less than 3 kg at the entry, i.e., of a diameter of about 11 cm.

The third fireball that fragmented under medium pressure was 2016 December 7. This fireball was, in fact, the most difficult to model. It was not possible to simultaneously fit the light curve and deceleration with the nominal set of parameters. There is a clear indication of fragmentation on the light curve at a height of 48 km under a pressure of 0.45 MPa. The deceleration after fragmentation corresponds to a fragment mass of ∼8 kg for the nominal values of $\Gamma A = 0.8$ and $\delta = 3400$ kg m^{-3}. However, the fireball brightness corresponds to a mass of less than 2 kg. The discrepancy was formally solved by assuming very low ΓA for some fragments, down to 0.45. It would physically mean an elongated shape and orientation with the smallest cross section in the direction of flight. Alternatively, a higher-than-nominal density (combined with a less elongated shape) or a lower luminous efficiency could be assumed. Such dramatic changes of nominal values were not needed for any other fireball. We have a suspicion that this meteoroid was not an ordinary chondrite. The spectrum of this fireball does not look exceptional and clearly excludes the meteoroid being an iron–nickel. The brightest lines belong to sodium and magnesium.

The fourth fireball with medium-pressure fragmentation was 2018 April 8. It was caused by a relatively large meteoroid with an initial mass of ∼70 kg (diameter ∼34 cm). A fragmentation at 0.65 MPa is well documented on the light curve and by one fragment seen on video. Other fragmentations then occurred at 1.1 and 1.4 MPa.

Generally, the analyzed fireballs document that the second-stage fragmentation can already start at 0.5 MPa or even earlier, especially for smaller meteoroids. The fact that the second stage occurred above 0.9 MPa for events with recovered meteorites can partly be a selection effect. More resistant meteoroids, which fragment later, can produce more or larger meteorites with higher chances for recovery. Nevertheless, even in the sample with no meteorites, the majority of severe second-phase fragmentations occurred above 0.9 MPa (Figure 7). Note that the largest meteoroid in this sample, 2017 November 14, showed no second-stage fragmentation. The last gross fragmentation occurred during the first phase at 0.09 MPa, where one slowly eroding and one regular fragment were produced. The regular fragment seems to survive pressures up to 2.2 MPa without further fragmentation and probably produced one large meteorite with a mass of about 10 kg. The shallow trajectory with a slope of only 15° to the horizontal was the reason why higher dynamic pressures were

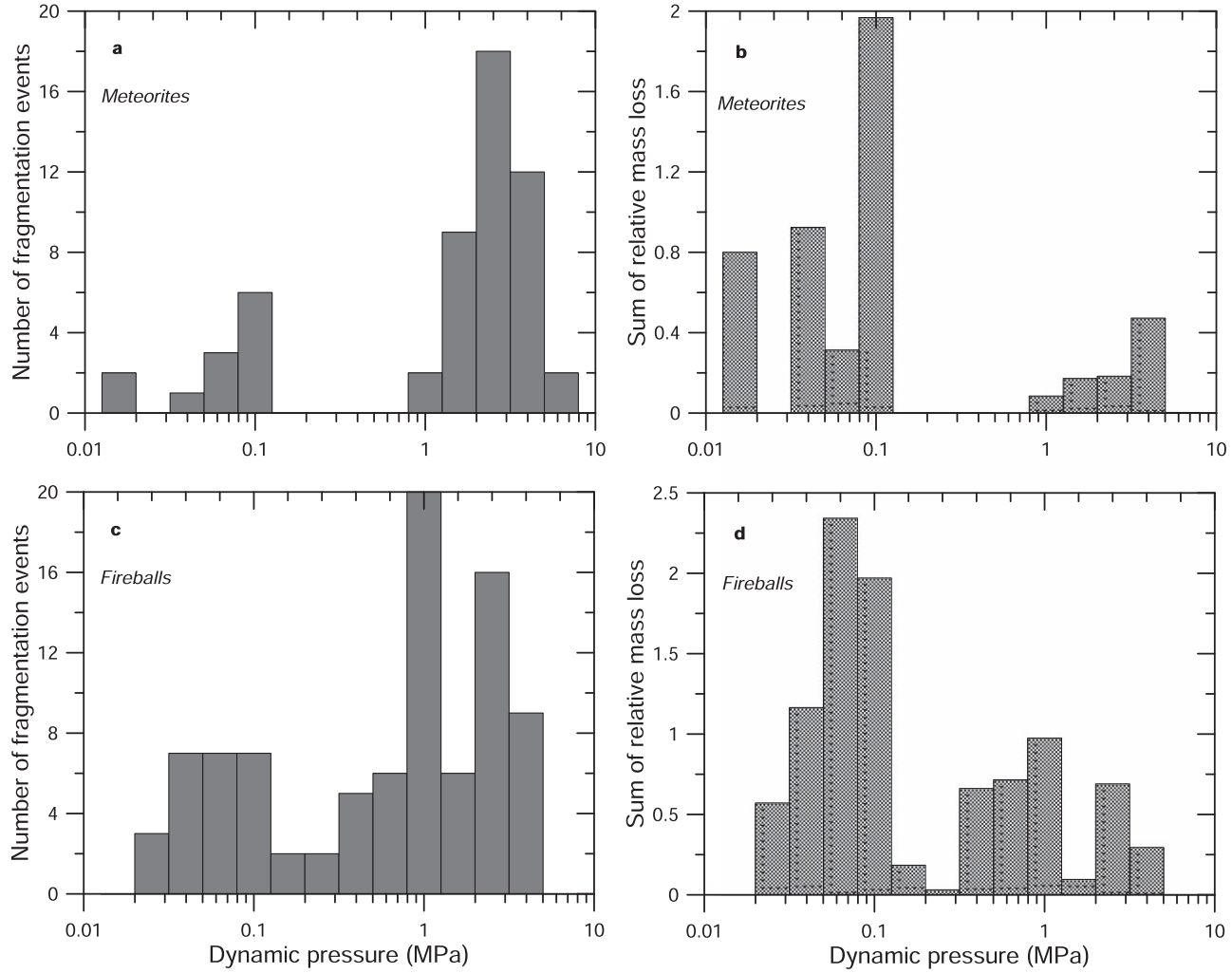

Figure 6. Histograms showing the distribution of dynamic pressures at gross-fragmentation points. Panels (a) and (b) are for recovered meteorite falls, and panels (c) and (d) are for fireballs with unrecovered meteorites. Panels (a) and (c) show the number of fragmentation events. In panels (b) and (d), the relative mass losses are summed (see the text for explanation).

not reached and the fragment was gently decelerated. This fireball lasted for 15 s.

The first phase of fragmentation occurred in all 14 fireballs. It was catastrophic, with $\gtrsim$60% mass loss, for six of them and nearly catastrophic, with ~50% mass loss, for the other four. Only four fireballs showed $\lesssim$30% mass loss during the first phase of fragmentation (see Figure 7(b)). The first phase occurred, with three exceptions, during the same range of dynamic pressures as for most recovered meteorite falls, i.e., 0.04–0.12 MPa. The small meteoroid 2018 January 18 fragmented already at 9 kPa, and the rather small meteoroid 2018 October 8 fragmented at 0.026 MPa. On the contrary, 2018 November 29 finished the first phase of fragmentation at 0.17 MPa. What is important, however, is that the two phases were well separated in almost all cases. After the first phase, there was a quiet period when the dynamic pressure increased more than 10 times (in 10 fireballs) or at least five times (in three fireballs) without further gross fragmentations. Only 2018 September 11 showed a very minor mass loss in between.

The light curve of fireball 2015 August 26, which is shown in Figure 3, is rather typical. The fireballs typically exhibit a sudden increase of brightness at the beginning, followed by a hump not expected for a single body but without further strong irregularities. Only much later, flares accompanying the second phase of fragmentation occur. When imaged on video, the fireballs also show typical changes of morphology. A long wake develops in the first half of the trajectory. The wake then disappears, and the bolide again becomes pointlike. Toward the end, a short wake is formed, which then separates into individually moving fragments. These changes are consistent with two phases of fragmentation. The initial wake must be formed by small dust particles. Large fragments move together for some time, since their deceleration is negligible at high altitudes. They can be separated at lower heights, where disruptions of the second phase also occur. A more detailed investigation of the initial wakes revealed that they indeed form at a time when fragmentation is indicated by the light curve (Shrbený et al. 2020).

4.3. Orbits

To complete the information, the heliocentric orbits of the 14 studied fireballs are given in Table 4. They were computed by the analytical method of Ceplecha (1987) and are compared graphically with the orbits of the recovered meteorites in Figure 8. The orbital elements of the meteorites can be found in the original publications. Their perihelia lie in the Venus–Earth

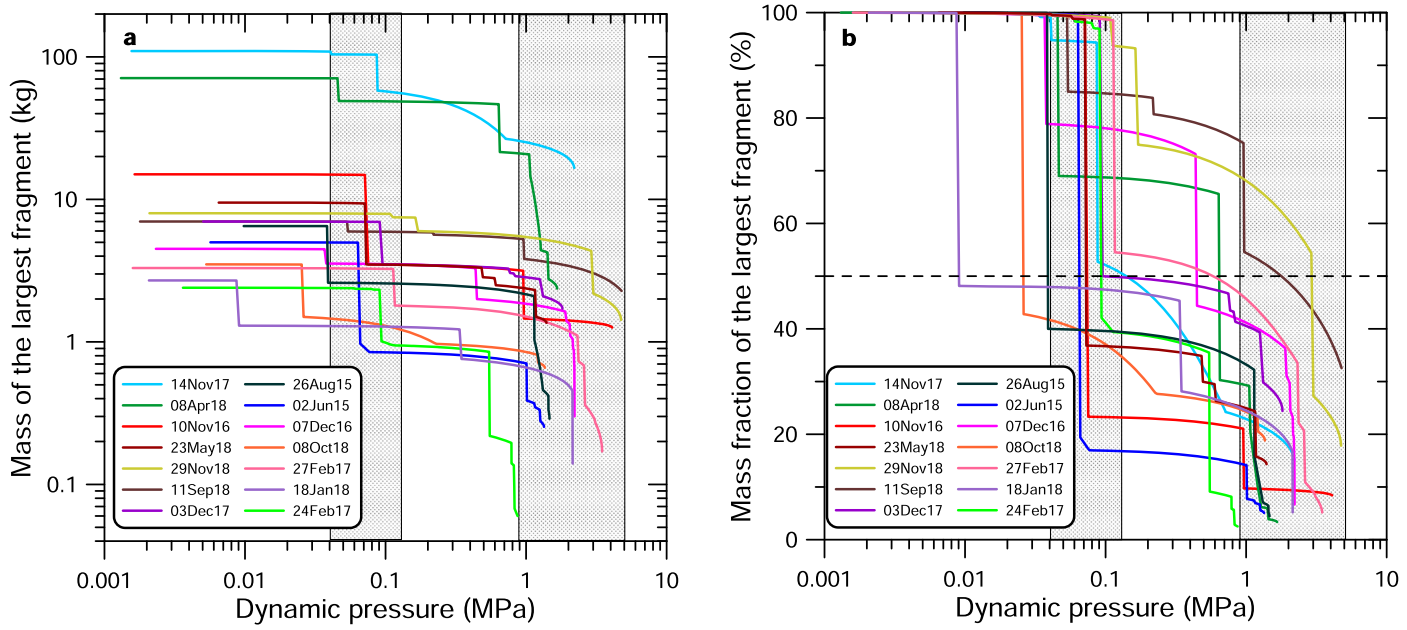

Figure 7. Same as Figure 5 for 14 fireballs classified as ordinary chondrite meteorite falls but where meteorites remained unrecovered.

region, and the aphelia are located between the orbits of Mars and Jupiter, in most cases closer to Mars. Except for Renchen, the inclinations are smaller than 10°.

The orbits of fireballs generally have the same character. In three cases, the aphelia are within the orbit of Mars; one of these orbits is of the Athen type. On the opposite side, three fireballs had semimajor axes around 2.7 au and aphelia around 4.5 au. This type of orbit is similar to that of the Košice meteorite. One fireball had a low perihelion distance of 0.35 au, and two had inclinations above 30°. Low perihelion or high inclination leads to a higher encounter velocity with the Earth. Meteoroids in these orbits encounter the same dynamic pressure at higher altitudes than meteoroids in orbits with low eccentricities and inclinations and are therefore somewhat disqualified for meteorite survival.

The Tisserand parameters relative to Jupiter are, for some fireballs, close to or even slightly below the border value of 3. Nevertheless, there is an overlap of comets and asteroids in this border region (Tancredi 2014), and since all aphelia are well within the orbit of Jupiter, we can classify all orbits as asteroidal.

4.4. Strewn Fields

The computed coordinates of the strewn fields of the 14 studied fireballs are given in Table 5. They are provided for the case where a meteorite is recovered in the future. The coordinates will enable the meteorite association with one of these fireballs.

For each fireball, the coordinates and approximate mass of the largest expected meteorite are given first. The coordinates were determined by dark flight computation using the method of Ceplecha (1987). The starting values were based on the observed trajectory and dynamics at the end of the fireball, fitted by the semiempirical model. Atmospheric winds were taken from the ALADIN numerical weather model forecast for the nearest hour and the nearest grid point to the fireball end, kindly provided by R. Brožková from the Czech Hydrometeorological Institute. Only for the 2018 January 18 fireball were the radiosonde measurements from Prague (12 UT) taken (this fall was unfavorable for searches because of low meteorite mass and very strong gusty winds, which made the landing point predictions uncertain in any case).

The strewn field is further described by the computed positions of representative smaller fragments, whose existence was inferred from the fragmentation modeling, primarily from light-curve fitting. In cases of fireballs 2017 December 3, 2018 April 8, and 2018 May 23, the positions of fragments directly seen in videos are included (two, three, and four fragments, respectively, in addition to the main piece). In practice, the meteorites can be spread along the central line defined by the listed coordinates but also several km to the sides, as the experience with well-described strewn fields with numerous meteorites shows (e.g., Gnos et al. 2009).

5. Discussion

We have shown that fragmentation events during falls of ordinary chondrites do not occur randomly but in two distinct phases. The first phase occurs at the early stages of the atmospheric flight, typically under dynamic pressures of 0.04–0.12 MPa. In some cases, the fragmentation had already started at about 0.01 MPa. The first phase was detected in all studied fireballs. In about two-thirds of cases, it was catastrophic or nearly catastrophic, i.e., more than 40% of mass was separated from the main body. The first phase was followed by a quiet period with no or only minor fragmentations. The second phase started at dynamic pressures between 0.9 and 5 MPa, and in some cases, especially in smaller meteoroids, at about 0.5 MPa or even earlier. On the other hand, the second phase was sometimes not observed at all. In these cases, however, the meteoroids were decelerated before the dynamic pressure reached 5 MPa.

5.1. Comparison with Carbonaceous Chondrites

We emphasize that carbonaceous chondrites behave differently. The recently modeled CM2 meteorite fall Maribo (2009 January 17) exhibited numerous fragmentations along most of

Table 4
Geocentric Radiants and Heliocentric Orbits of Fireballs Analyzed in This Study (J2000.0)

Name	α_G (deg)	δ_G (deg)	v_G (km s^{-1})	a (au)	e	q (au)	Q (au)	i (deg)	ω (deg)	Ω (deg)	T_{Jup}	Mass (kg)
2015 Jun 2	232.70	26.37	11.88	1.794	0.471	0.9489	2.64	13.69	216.95	71.842	3.91	5
	±0.02	0.03	0.07	0.012	0.004	0.0002	0.02	0.08	0.04		0.02	
2015 Aug 26	314.77	−6.99	16.00	2.668	0.6986	0.8041	4.53	4.496	239.77	153.207	2.97	6.5
	0.02	0.02	0.03	0.012	0.0015	0.0004	0.03	0.016	0.03		0.01	
2016 Nov 10	43.53	66.513	20.82	1.282	0.4691	0.6804	1.883	30.46	268.84	227.891	4.82	15
	0.06	0.006	0.06	0.003	0.0015	0.0004	0.007	0.09	0.09		0.01	
2016 Dec 7	78.56	16.82	18.17	1.432	0.594	0.5821	2.283	3.855	95.61	75.289	4.47	4.5
	0.03	0.03	0.07	0.004	0.002	0.0013	0.010	0.003	0.06		0.01	
2017 Feb 24	145.75	17.93	13.65	1.736	0.538	0.8027	2.67	1.622	242.70	336.106	3.97	2.4
	0.03	0.03	0.07	0.011	0.003	0.0005	0.02	0.016	0.05		0.02	
2017 Feb 27	171.656	6.362	29.39	2.249	0.8421	0.3552	4.143	3.067	293.78	338.442	3.02	3.3
	0.006	0.008	0.03	0.007	0.0006	0.0003	0.014	0.012	0.02		0.01	
2017 Nov 14	36.86	2.04	16.00	2.59	0.694	0.7913	4.39	5.419	59.21	52.284	3.02	110
	0.04	0.05	0.07	0.03	0.004	0.0005	0.06	0.007	0.02		0.02	
2017 Dec 3	40.34	66.802	7.19	1.119	0.1974	0.8981	1.340	9.80	242.56	251.479	5.55	7
	0.14	0.009	0.05	0.002	0.0015	0.0002	0.004	0.06	0.15		0.01	
2018 Jan 18	166.17	77.396	16.63	1.501	0.4052	0.89252	2.109	25.40	227.33	298.365	4.35	2.7
	0.03	0.006	0.02	0.002	0.0007	0.00003	0.004	0.02	0.03		0.01	
2018 Apr 8	252.72	48.17	11.89	0.9888	0.0962	0.8936	1.0839	22.23	283.1	18.634	6.07	71
	0.03	0.02	0.03	0.0007	0.0002	0.0005	0.0010	0.05	0.5		0.01	
2018 May 23	43.35	78.91	6.61	1.112	0.1501	0.9453	1.279	10.52	119.4	62.391	5.58	9.5
	0.21	0.09	0.05	0.002	0.0014	0.0002	0.004	0.08	0.4		0.01	
2018 Sep 11	334.594	18.20	20.87	2.639	0.7344	0.7007	4.58	16.68	253.60	168.851	2.90	7
	0.008	0.02	0.04	0.015	0.0016	0.0003	0.03	0.03	0.02		0.01	
2018 Oct 8	347.694	11.27	8.35	1.410	0.3681	0.8909	1.929	3.82	233.31	195.216	4.66	3.5
	0.013	0.04	0.03	0.003	0.0014	0.0003	0.006	0.02	0.01		0.01	
2018 Nov 29	356.91	81.618	23.33	2.429	0.6301	0.89854	3.959	35.56	219.70	246.617	3.01	8
	0.05	0.012	0.03	0.008	0.0012	0.00006	0.016	0.04	0.02		0.01	

Note. The Tisserand parameter relative to Jupiter and the initial mass from the model are also given.

the trajectory (Borovička et al. 2019b). The first significant mass loss occurred at 0.017 MPa, and further disruptions accompanied by large-amplitude flares followed at 0.25–4.3 MPa, i.e., at a wide range of pressures. We identified one similar case among bright fireballs observed by the EN (though much fainter than Maribo). The light curve of that fireball, EN160517_205435, is shown in Figure 9. There were numerous flares in the second half of the trajectory at dynamic pressures of 0.28–1.37 MPa. The shape of the light curve suggests that a minor early fragmentation occurred as well, possibly at 0.008 MPa. The behavior was similar to Maribo and rather distinct from other fireballs in this study in the sense that there were numerous well-defined flares covering the whole second half of the light curve. According to the PE criterion of Ceplecha & McCrosky (1976), the fireball was classified as type II. It is therefore probable that it was a carbonaceous chondrite. The multiflare behavior may be characteristic for carbonaceous chondrites, although more data are obviously needed because Maribo is the only confirmed and well-studied carbonaceous fall. The entry mass of EN160517_205435 from the model was 19 kg, and the modeling showed that no meteorites larger than a few g can be expected. The entry speed was 20.61 km s^{-1}, and the orbit was asteroidal.

5.2. Cracks as the Cause of the Second Phase of Fragmentation

The fragments of ordinary chondrites subject to the second phase of fragmentation have strengths of 0.9–5 MPa, which is about an order of magnitude lower than the tensile strength of ordinary chondritic meteorites (20–40 MPa; Slyuta 2017; Flynn et al. 2018; Ostrowski & Bryson 2019). Cracks resulting from collisions between asteroids (or meteoroids) in interplanetary space can naturally explain such a decrease of strength in comparison with (nearly) pristine rock. Note that the analysis of Maribo showed that cracks do not play an important role in carbonaceous chondrites. The reason why carbonaceous chondrites fragment under a wide range of pressures is probably that carbonaceous meteoroids are highly inhomogeneous and contain parts with different degrees of compactness and different strengths (Borovička et al. 2019b). Different types of asteroidal material, which have no meteorite analog, also exist. An example was the Romanian superbolide of 2015 January 7, which remained almost intact until 1 MPa and then was quickly pulverized (Borovička et al. 2017).

The important question is what the reason for the first phase of fragmentation is. Since there is a huge gap (often about an order of magnitude) in strength between the two phases, it is very unlikely that cracks are responsible for the first phase as well. Naturally, cracks of different widths and 3D shapes can be expected to exist and lead to different fragmentation strengths. However, there should be a smooth distribution of crack strengths. The distribution probably covers the second phase, i.e., 0.9–5 MPa, in some cases, especially in small meteoroids, extending down to 0.5 MPa. Note that according to the widely used Weibull (1951) distribution, the strength of terrestrial rock decreases with size. Meteoroids seem to behave differently. We speculate that the reason for the lower strength of smaller meteoroids may be that wide cracks producing low

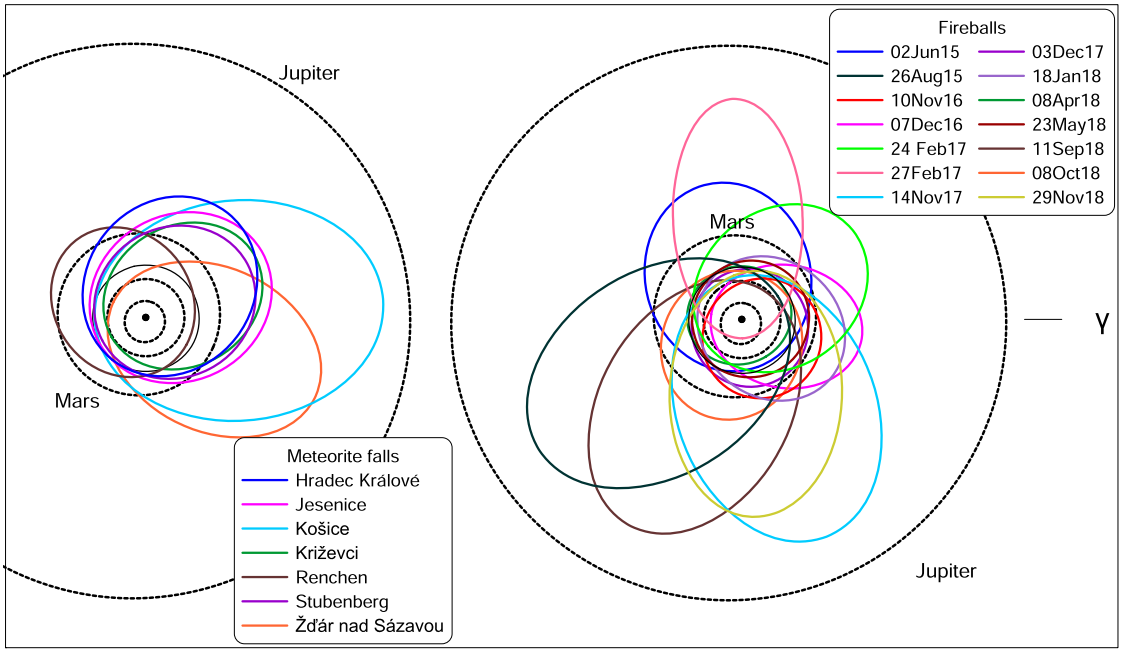

Figure 8. Orbits of the meteorites (left) and fireballs with unrecovered meteorites (right) in the projection to the ecliptic plane. Orbits of planets, except the Earth, are dotted. The vernal equinox is to the right.

strength have a higher probability in small meteoroids to go across the whole body.

5.3. The First Phase of Fragmentation

The first phase needs to be caused by a different mechanism. A clue may be the Benešov superbolide, which dropped individual meteorites of at least two different types, LL3.5 and H5 (Spurný et al. 2014). The meteoroid was therefore an assembly of debris of at least two different asteroids. In this respect, it was similar to the Almahata Sitta meteorite fall, which contained even more meteorite types (Bischoff et al. 2010; Shaddad et al. 2010). The Benešov meteorite fall was observed by the EN in 1991. Unfortunately, there were no radiometers at that time, and the photographic light curve is not detailed and precise enough for reliable modeling by the semiempirical model. From the deceleration at high altitudes, it is, nevertheless, clear that the meter-sized meteoroid disrupted into smaller pieces early in the flight. The most likely scenario was discussed by Borovička (2016) and is depicted in Figure 5, together with other meteorite falls discussed in this paper. The first Benešov disruption most likely occurred at a dynamic pressure of 0.05 MPa, i.e., within the range for the first phase of fragmentation. This can lead to the hypothesis that the strength of the first phase of fragmentation corresponds to the strength with which foreign pieces are held together.

There is no evidence that other meteoroids studied here were composed of pieces of different composition. Nevertheless, chemically and mineralogically homogeneous meteoroids can be composed of pieces that were completely separated during asteroid collisions and then reassembled. Most of the currently existing asteroids in the size range 200 m–10 km are considered to be gravitational aggregates: so-called rubble piles (Pravec & Harris 2000; Hestroffer et al. 2019). The strength is therefore near zero. If intergrain van der Waals forces are considered, the strength can reach about 25 Pa (Sánchez & Scheeres 2014). That is still much lower than observed for the first phase of fragmentation. Individual components of meteoroids and small asteroids such as Benešov and Almahata Sitta (=asteroid 2008 TC_3) must therefore be somehow cemented together so that the resulting strength is of the order of 50–100 kPa.

5.4. Formation of Low-strength Meteoroids

We can only speculate what the cementing can look like. The gravitational reassembly is not supposed to occur in free space, since the mutual gravity of meter-sized or smaller bodies is too low. Instead, the debris was probably first accumulated on the surface of a larger asteroid, which possibly became subsurface after fallout of more material. Partial impact melting of the debris and the adjacent dust grains could cement the material together. The pressure from upper layers could further help. Note that the cementing we are speaking about is relatively weak, only about two times stronger than the tensile strength of snow (which was measured to be ~0.01–0.04 MPa by Upadhyay et al. 2007).

The formed breccia resided on the asteroid until further asteroid collision, which finally ejected decimeter- and meter-sized fragments into free space. Such a multifragmentation history was discussed (Horstmann & Bischoff 2014; Goodrich et al. 2015) for Almahata Sitta, which, nevertheless, is not an ordinary chondrite but predominantly a ureilite. Goodrich et al. (2015) proposed that Almahata Sitta (2008 TC_3) originated from the outer layers of regolith of its immediate parent body and that other polymict ureilites, which did not disintegrate into individual mineralogically distinct components during the atmospheric flight, came from a deeper regolith of the same body. Goodrich et al. (2019) identified two friable and mineralogically diverse Almahata Sitta meteorites probably representing the bulk material of 2008 TC_3, the material that was mostly lost during the atmospheric flight and encompassed the harder material, which more easily survived as meteorites.

Our study indicates that a history of multiple fragmentation and reaccumulation in interplanetary space is also typical for

Table 5
Computed Strewn Field Coordinates

Fireball	Longit. (°E)	Latit. (°N)	Mass (g)	Fireball	Longit. (°E)	Latit. (°N)	Mass (g)	Fireball	Longit. (°E)	Latit. (°N)	Mass (g)
2015 Jun 2	11.9976	50.1005	200	2017 Feb 27	14.4319	49.6985	40	2018 May 23	17.1457	49.5317	800
	12.0086	50.0890	30		14.4143	49.6754	10		17.1533	49.5521	250
	12.0280	50.0755	3	2017 Nov 14	7.0167	50.2652	11500		17.1501	49.5733	60
2015 Aug 26	12.4681	49.0922	125		7.7850	50.2040	5		17.1485	49.5856	20
	12.4517	49.0600	25	2017 Dec 3	14.4315	48.9888	1350		17.1471	49.5952	10
	12.4445	49.0318	4		14.4457	48.9957	400	2018 Sep 11	15.6217	47.3554	40
2016 Nov 11	21.0824	48.2894	1100		14.4969	49.0122	10		15.6332	47.3145	2
	21.0778	48.3153	150	2018 Jan 18	14.5027	49.3063	100	2018 Oct 8	14.1967	50.3590	500
	21.0798	48.3338	40		14.5421	49.3165	20		14.2330	50.3128	8
2016 Dec 7	15.2182	49.7128	130		14.6433	49.3430	5	2018 Nov 29	16.6016	45.8450	900
	15.1545	49.6997	10	2018 Apr 8	16.5482	46.0773	1800		16.5991	45.8873	30
	15.1007	49.6843	2		16.5845	46.1058	600				
2017 Feb 24	13.2668	48.5415	40		16.5917	46.1116	500				
	13.4115	48.5154	2		16.6400	46.1483	120				
					16.7213	46.2060	10				

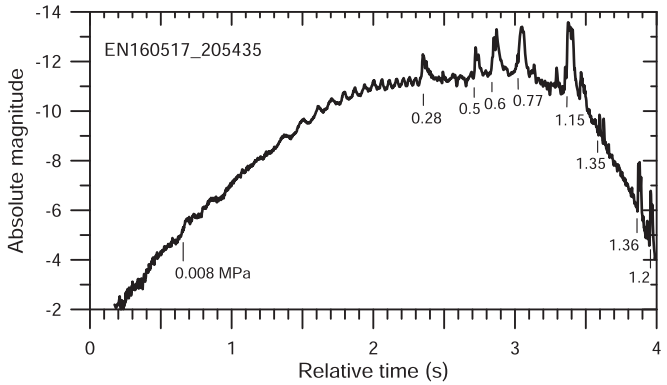

Figure 9. Radiometric light curve of type II fireball EN160517_205435. Points of main fragmentations and the corresponding dynamic pressures in MPa are indicated.

ordinary chondrites, even if foreign material is not present and all reaccumulated material originated from the same source. As a result of this process, the bulk strength of decimeter- and meter-sized meteoroids was found to be in the range of 0.04–0.12 MPa or even less. It depends on the actual size of the building blocks whether the initial disruption is catastrophic or only a small part of the mass is lost. The same properties can be expected for larger bodies of the size of tens of m. Nevertheless, no evidence was found for fragmentation in the first half of the trajectory of the ordinary chondritic 19 m Chelyabinsk impactor, except some release of dust forming an atmospheric dust trail (Borovička 2016). However, the data, especially light-curve, are of lower quality, not comparable with radiometric curves. Moreover, detection of early atmospheric fragmentation of bodies of this size may be difficult. Shuvalov et al. (2017) demonstrated that a strengthless body will produce an almost identical light curve in the upper part of the trajectory as the real object.

6. Summary

In this paper, we presented the semiempirical model of atmospheric fragmentation of meteoroids and its application to seven confirmed meteorite falls and 14 fireballs with predicted but unrecovered meteorites. All recovered meteorites were ordinary chondrites. Of the unrecovered meteorites, at least 13 are expected on the basis of fall statistics to be ordinary chondrites. We provided additional information, orbits and strewn fields, for the fireballs. Details about the meteorite falls can be found in the original papers.

The fact that the strength of meteoroids is significantly lower than the strength of meteorites measured in the laboratory was already emphasized by Popova et al. (2011). The new results of this study are that meteoroid strengths are not distributed randomly but are predominantly concentrated in two regions (marked B and C below). When combined with the data on meteorites and medium-sized asteroids, we conclude that ordinary chondritic material and bodies can be found in four strength categories. Their typical tensile/fragmentation strength and probable physical structure is as follows.

A (20–40 MPa). Pristine material or compact breccias formed in asteroids at high pressures. They can be encountered as meteorites, i.e., the strongest parts of meteoroids, which survived the atmospheric passage. Only rarely can the whole meteoroid be of this type (the example is Carancas). Microscopic cracks can be present.

B (0.5–5 MPa). Cracked material. Macroscopic cracks were formed during asteroid collisions in interplanetary space. The body fragments along the cracks into category A material during the atmospheric flight when the dynamic pressure reaches the strength value. In favorable conditions (low entry speed and shallow angle), the dynamic pressure may not reach the strength value, and the body can land as a meteorite.

C (0.04–0.12 MPa). Reassembled and cemented material. According to our hypothesis, which needs to be tested, this strength category corresponds to material that was secondarily formed from the debris of asteroid collisions (of categories A and B) cemented together on the surface or near-surface layers of asteroids. During subsequent collisional evolution, the layers were destroyed and their parts were released into interplanetary space as individual meteoroids. During the atmospheric entry, they are separated early into the A and B category components.

D (~0 Pa). Reassembled material held together only by mutual gravity or van der Waals forces. This category corresponds to rubble-pile asteroids. Meteoroids of type D have not been observed.

The fact that most of the meteoroids are weakly cemented aggregates of cracked material is the reason why the terrestrial atmosphere effectively protects us against meteoroid impacts. For example, a 1000 kg meteoroid of category A entering at 15 km s^{-1} with an entry angle of 45° would produce a 600 kg meteorite (assuming the nominal ablation coefficient of 0.005 kg MJ^{-1}). But the reality is different. In a typical case, hundreds of mostly small meteorites of total mass less than 100 kg are produced instead.

The authors acknowledge the work of all operators and technicians who are keeping the observatories of the European Fireball Network and the associated infrastructure running. Special thanks go to J. Svoreň (Astronomical Institute of the Slovak Academy of Sciences) and the late H. Mucke (Österreichische Astronomische Verein) for their support of the network in Slovakia and Austria, respectively. We are indebted to R. Brožková (Czech Hydrometeorological Institute, CHMI) for providing us the meteorological models needed for dark flight computation. We thank D. Ščerba, L. Ronge (CHMI), D. Šegon (Croatian Meteor Network), W. Stelzig, and M. Landy Gyebnar for providing their fireball images or videos for analysis. We appreciate the tireless meteorite searching by R. Sporn and M. Neuhofer and the coordination work of D. Heinlein. This work was supported by grant 19-26232X from the Czech Science Foundation (GA ČR). The recent modernization of the network, crucial for this work, was funded from the Praemium Academiae of the Czech Academy of Sciences. The institutional research plan is RVO:67985815.

ORCID iDs

Jiří Borovička https://orcid.org/0000-0002-5569-8982

References

Baldwin, B., & Sheaffer, Y. 1971, JGR, 76, 4653
Bischoff, A., Barrat, J.-A., Bauer, K., et al. 2017, M&PS, 52, 1683
Bischoff, A., Barrat, J.-A., Berndt, J., et al. 2019, ChEG, 79, 125525
Bischoff, A., Horstmann, M., Pack, A., et al. 2010, M&PS, 45, 1638
Bischoff, A., Jersek, M., Grau, T., et al. 2011, M&PS, 46, 793
Bland, P. A., & Artemieva, N. A. 2006, M&PS, 41, 607
Borovička, J. 1990, BAICz, 41, 391
Borovička, J. 2016, in IAU Symp. 318, Asteroids: New Observations, New Models, ed. S. R. Chesley (Cambridge: Cambridge Univ. Press), 80
Borovička, J., & Kalenda, P. 2003, M&PS, 38, 1023
Borovička, J., Macke, R., Campbell-Brown, M. D., et al. 2019a, in Meteoroids: Sources of Meteors on Earth and Beyond, ed. G. O. Ryabova et al. (Cambridge: Cambridge Univ. Press), 37
Borovička, J., Popova, O., & Spurný, P. 2019b, M&PS, 54, 1024
Borovička, J., & Spurný, P. 2008, A&A, 485, L1
Borovička, J., Spurný, P., Brown, P., et al. 2013a, Natur, 503, 235
Borovička, J., Spurný, P., Grigore, V. I., & Svoreň, J. 2017, P&SS, 143, 147
Borovička, J., Spurný, P., & Koten, P. 2007, A&A, 473, 661
Borovička, J., Spurný, P., & Shrbený, L. 2019c, in Proc. Int. Meteor Conf. Pezinok-Modra, ed. R. Rudawska (Hove: Int. Meteor Org.), 28, https://imc2018.imo.net/proceedings/Dfty56ghu52559aidDZZ897/IMC2018_Proceedings.pdf
Borovička, J., Spurný, P., Šegon, D., et al. 2015, M&PS, 50, 1244
Borovička, J., Tóth, J., Igaz, A., et al. 2013b, M&PS, 48, 1757
Brown, P., ReVelle, D. O., Silber, E. A., et al. 2008, JGRE, 113, E09007
Ceplecha, Z. 1987, BAICz, 38, 222
Ceplecha, Z., Borovička, J., Elford, W. G., et al. 1998, SSRv, 84, 327
Ceplecha, Z., & McCrosky, R. E. 1976, JGR, 81, 6257
Ceplecha, Z., Spurný, P., Borovička, J., & Keclíková, J. 1993, A&A, 279, 615
Fadeenko, Yu. I. 1967, FizGV, 3, 276
Flynn, G. J., Consolmagno, G. J., Brown, P., & Macke, R. J. 2018, ChEG, 78, 269
Fry, C., Melanson, D., Samson, C., et al. 2013, M&PS, 48, 1060
Gattacceca, J., Bouvier, A., Grossman, J., Metzler, K., & Uehara, M. 2019, M&PS, 54, 469
Gnos, E., Lorenzetti, S., Eugster, O., et al. 2009, M&PS, 44, 375
Goodrich, C. A., Hartmann, W. K., O'Brien, D. P., et al. 2015, M&PS, 50, 782
Goodrich, C. A., Zolensky, M. E., Fioretti, A. M., et al. 2019, M&PS, 54, 2769
Hestroffer, D., Sánchez, P., Staron, L., et al. 2019, A&ARv, 27, 6
Hills, J. G., & Goda, M. P. 1993, AJ, 105, 1114
Holsapple, K. A. 2009, P&SS, 57, 127
Horstmann, M., & Bischoff, A. 2014, ChEG, 74, 149
Jenniskens, P., Betlem, H., Betlem, J., et al. 1994, Metic, 19, 246
Kalasová, D., Zikmund, T., Spurný, P., et al. 2020, M&PS, in press
Oberst, J., Molau, S., Heinlein, D., et al. 1998, M&PS, 33, 49
Ostrowski, D., & Bryson, K. 2019, P&SS, 165, 148
Pecina, P., & Ceplecha, Z. 1983, BAICz, 34, 102
Picone, J. M., Hedin, A. E., Drob, D. P., & Aikin, A. C. 2002, JGRA, 107, 1468
Popova, O., Borovička, J., & Campbell-Brown, M. D. 2019, in Meteoroids: Sources of Meteors on Earth and Beyond, ed. G. O. Ryabova et al. (Cambridge: Cambridge Univ. Press), 9
Popova, O., Borovička, J., Hartmann, W. K., et al. 2011, M&PS, 46, 1525
Pravec, P., & Harris, A. W. 2000, Icar, 148, 12
Register, P. J., Mathias, D. L., & Wheeler, L. F. 2017, Icar, 284, 157
ReVelle, D. O., & Ceplecha, Z. 2001, in ESA-SP 495, Proc. Meteoroids 2001 Conf., ed. B. Warmbein (Noordwijk: ESA), 507
Richardson, D. C., Bottke, W. F., & Love, S. G. 1998, Icar, 134, 47
Robertson, D. K., & Mathias, D. L. 2017, JGRE, 122, 599
Sánchez, P., & Scheeres, D. J. 2014, M&PS, 49, 788
Shaddad, M. H., Jenniskens, P., Numan, D., et al. 2010, M&PS, 45, 1557
Shrbený, L., Spurný, P., & Borovička, J. 2020, P&SS, 187, 104956
Shuvalov, V., Svetsov, V., Popova, O., & Glazachev, D. 2017, P&SS, 147, 38
Simonenko, A. N. 1973, Metik, 32, 50
Slyuta, E. N. 2017, SoSyR, 51, 64
Spurný, P., Borovička, J., Baumgarten, G., et al. 2017a, P&SS, 143, 192
Spurný, P., Borovička, J., Haloda, J., et al. 2016, LPICo, 1921, 6221
Spurný, P., Borovička, J., Kac, J., et al. 2010, M&PS, 45, 1392
Spurný, P., Borovička, J., Mucke, H., & Svoreň, J. 2017b, A&A, 605, A68
Spurný, P., Borovička, J., & Shrbený, L. 2007, in IAU Symp. 236, Near Earth Objects, Our Celestial Neighbors: Opportunity and Risk, ed. G. B. Valsecchi et al. (Cambridge: Cambridge Univ. Press), 121
Spurný, P., Borovička, J., & Shrbený, L. 2020, M&PS, 55, 376
Spurný, P., Haloda, J., Borovička, J., et al. 2014, A&A, 570, A39
Svetsov, V. V., Nemtchinov, I. V., & Teterev, A. V. 1995, Icar, 116, 131
Tancredi, G. 2014, Icar, 233, 66
Tóth, J., Svoreň, J., Borovička, J., et al. 2015, M&PS, 50, 853
Trigo-Rodríguez, J. M., & Llorca, J. 2006, MNRAS, 372, 655
Upadhyay, A., Joshi, S. K., & Chandel, C. 2007, DSJ, 57, 787
Vojáček, V., Borovička, J., Spurný, P., Čapek, D., et al. 2020, P&SS, 184, 104882
Weibull, W. A. 1951, JAM, 18, 293